metals

Article

Optimization of Direct Laser Deposition of a Martensitic Steel Powder (Metco 42C) on 42CrMo4 Steel

André A. Ferreira [1,2,*], Roya Darabi [1,2], João P. Sousa [2], João M. Cruz [3], Ana R. Reis [1,2] and Manuel F. Vieira [1,2,*]

1 Faculty of Engineering, University of Porto, 4200-465 Porto, Portugal; rdarabi@inegi.up.pt (R.D.); areis@inegi.up.pt (A.R.R.)
2 LAETA/INEGI—Institute of Science and Innovation in Mechanical and Industrial Engineering, 4200-465 Porto, Portugal; jpsousa@inegi.up.pt
3 SERMEC-Group, 4425-348 Folgosa-Maia, Portugal; joaocruz@sermecgroup.pt
* Correspondence: andreferreira@fe.up.pt (A.A.F.); mvieira@fe.up.pt (M.F.V.); Tel.: +351-9-1046-1480 (A.A.F.)

Abstract: In this study, the deposition of martensitic stainless-steel (Metco 42C) powder on 42CrMo4 structural steel by direct laser deposition (DLD) was investigated. Clads were produced by varying the laser power, scanning speed, feed rate, and preheating. The effect of these processing variables on the microstructure and microhardness of the clads was analyzed, as well as their soundness, yield (measured by dilution), and geometric characteristics (height, width, and depth). The complex interaction of the evaluated processing variables forced the application of complex parameters to systematize their effect on the clads. A genetic optimization algorithm was performed to determine the processing conditions warranting high-quality clads, that is, sound clads, metallurgically bonded to the substrate with required deposition yield.

Keywords: direct laser deposition; microstructure; EBSD; martensitic stainless steel; preheating; optimization

check for updates

Citation: Ferreira, A.A.; Darabi, R.; Sousa, J.P.; Cruz, J.M.; Reis, A.R.; Vieira, M.F. Optimization of Direct Laser Deposition of a Martensitic Steel Powder (Metco 42C) on 42CrMo4 Steel. *Metals* **2021**, *11*, 672. https://doi.org/10.3390/met11040672

Academic Editors: Takayoshi Nakano and Evgeny A. Kolubaev

Received: 2 March 2021
Accepted: 16 April 2021
Published: 20 April 2021

1. Introduction

Direct Laser Deposition (DLD) is one of the laser-based additive manufacturing (LBAM) processes investigated for additive metal part manufacture, repair, and reconstruction. DLD uses a laser beam as an energy source to melt metallic powders, manufacture parts layer by layer, and repair or cladding components by depositing one or a few layers. This technique has many advantages compared to conventional processes, such as arc welding, due to the production of better bead/layers with the controlled thermal distribution, promoting a lower heat-affected zone (HAZ), less dilution, minimum distortion, and better surface quality, which ensures a superior resistance to wear and corrosion [1–4].

The repair/remanufacturing of metallic components is one of the main applications of DLD. The use of suitable addition materials and process parameters allows the production of precise, durable, and high-quality repairs with properties similar or superior to those of the substrate, contributing to sustainable industrial development. The deposited layers have excellent metallurgical bonding, the heat-affected zone (HAZ) is small with adequate heat transfer control, dilution is minimal (evaluated through the extension of the remelted region with mixing between cladding and substrate materials) and allows localized repair of parts in difficult-to-reach places [5–8]. Moreover, innovative material systems can be used to produce complex components in which the chemical composition of the individual layers is gradually changed, adjusting them to the desired properties of the component [9].

Due to its characteristics, DLD is one of the most attractive and competitive component repair processes, being applied in industrial sectors as diverse as aeronautics, petrochemical (offshore), energy, transport, and defense, among others. Examples of products that can be repaired by DLD include gearboxes, gears, blowers, combustion engine parts, couplings, pumps, shafts, turbine parts, and rollers [10].

The geometry of the cladding (height, depth, and length) is directly related to physical phenomena, such as the Marangoni effect in the melt pool, which results from the interaction of the laser beam with the powder and the substrate [10,11]. Several studies correlated the thermal effects, in the melt pool and in the heat-affected zone (HAZ), with the structure and the mechanical and tribological properties of the laser cladding [12–14]. Although theoretical and experimental studies have developed relevant information about DLD, there are still many challenges, such as process optimization, 3D reconstruction of highly complex structures, and substrate preheating, which need to be clarified.

The laser processing parameters, laser power, scanning speed, and feed rate, directly correlate with melt pool geometry, strongly influencing claddings properties. Of the most important processing parameters in DLD processes, the laser power has the largest influence on melt pool size, with its size increasing almost linearly with laser power [15]. There is no formation of the melt pool for low laser power and high feed rate due to the absorption of the laser beam energy by the powder particles. However, for low feed rate and high laser power, significant melting of the substrate occurs, which compromises the cladding properties [16–18]. The laser power also significantly affects the HAZ [19]. The scanning speed and the powder feed rate have an interactive effect on the melt pool geometry and the HAZ, weakening the primary impact of laser power [15,19,20]. However, the interaction among the processing parameters is highly affected by the characteristics of the powder/substrate system.

DLD still has a way to go for broader industrial sectors. The application of wear-resistant steel beads on substrates of low and medium carbon steels is an aspect that may be extensively used, either in component repair or in its cladding with a more resistant layer. The use of steel entails a careful analysis of the processing conditions. The high cooling rates that are characteristic of this process, due to the localized heat inputs by the laser beam, are responsible for metallurgical defects associated with metastable phases both in the deposited material and in the HAZ. Preheating (PHT) of the substrate is one of the processes able to reduce the cooling rate. PHT decreases hardness in HAZ [9], reduces the sharp thermal gradients [3], and increases the laser absorption rate by the substrate, improving the stress distribution and preventing the formation of hard structures that are harmful to the mechanical properties of the cladding [11]. As the best knowledge of authors, few studies in the literature on these steel/steel systems correlate the process parameters with the dilution, structure, and hardness of the cladding and base materials [21–27]. In these studies, the influence of processing conditions on wear resistance and corrosion of the clads produced was also analyzed.

In this study, martensitic stainless-steel powder, type AISI 431, was deposited on 42CrMo4 steel, varying the process parameters, with and without performing preheating. 42CrMo4 steel is often used to produce components, such as gears and main-shafts, and martensitic steel powder 431 is used in the repair/remanufacturing of these components by the SERMEC-Group. Single clad tracks were formed to evaluate the metallurgical and mechanical characteristics of the deposits. The influence of several process parameters, such as laser power, scanning speed, powder feed rate, and preheating, was analyzed to achieve the desired clad quality without cracking and structural imperfections. A genetic algorithm was used to optimize the height, depth, and dilution values and overcome the complex nature of the effects of the involved parameters on each other. Strategies were developed to guarantee the compatibility and the metallurgical bond between cladding and substrate, taking into account avoiding the structural defects like cracks, and exploring synergies between the properties of the utilized materials.

2. Materials and Methods

Water atomized martensitic stainless-steel powder (Metco 42C), similar to AISI 431, was used for deposition. Scanning electron microscopy (SEM) images show powder particles have an irregular (non-spheroidal) morphology with particles size range between 45 to 106 μm (Figure 1).

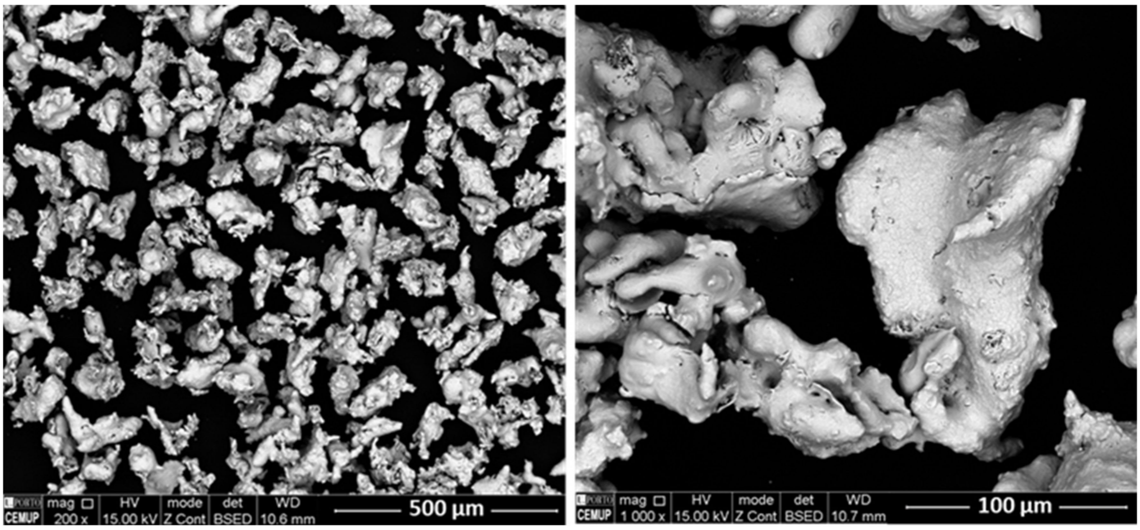

Figure 1. Scanning electron microscopy (SEM) images of martensitic stainless-steel powder (Metco 42C).

42CrMo4 steel was utilized as the substrate for depositions. 42CrMo4 is medium carbon steel with excellent fatigue and impact resistance, high mechanical strength and toughness, and good machinability. This material is classified as a low-alloy structural steel type and has a widespread application in manufacturing critical industrial components, such as gears, automotive parts, drilling joints for deep wells, and wind generators [28,29]. Its mechanical and chemical properties are described in standard EN 10,269 [30]. Chemical analysis of the Metco 42C powder and 42CrMo4 steel are shown in Table 1.

Table 1. Chemical composition of Metco 42C and 42CrMo4 steel (wt. %).

Materials	C	Cr	Ni	Mn	Mo	Si	P	S	Fe
Metco 42C	0.18	17.3	1.9	-	-	2.1	-	-	Bal.
42CrMo4	0.42	1.11	-	0.67	0.19	0.28	0.025	0.015	Bal.

Before deposition, the substrates were cleaned with pure acetone and preheated to approximately 300 °C by oxy torch, to decrease the cooling rate in melt pool and HAZ regions and eliminate moisture. The temperature was selected following welding practices for 42CrMo4 steel and controlled with a digital pyrometer gauge. The effect of preheating treatment (PHT) on microstructures, grain size, and formation of metastable phases (martensite) was evaluated.

The DLD machine consists of a modular coaxial processing head (Figure 2) and equipped with a fibre-coupled laser diode, model Laserline LDF 3000–100, with a nominal beam power of 6000 W. The powder nozzle is mounted on a KUKA KR 90 R3100 industrial robot, with six axes connected to the robot control unit.

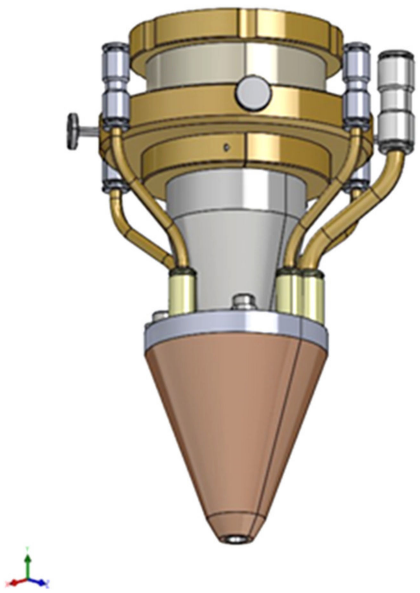

Figure 2. Coaxial configuration for powder feed.

The data of experiments was aquired through changes in the following parameters: laser power, scanning speed, powder feed rate, and preheating (PHT) as can be seen in Table 2. The terminology M_P_SS_FR was used to identify the samples, being: M—powder Metco 42C; P—laser power (kW); SS—scanning speed (mm/s); FR—feed rate (g/min). Then, the feed-driven results from experiments were employed on the implementation of the Genetic algorithm in order to the optimization of the process.

Table 2. Samples and parameters used to optimize the DLD process.

Sample	P (kW)	SS (mm/s)	FR (g/min)
M_1_2_15	1	2	15
M_1_6_15	1	6	15
M_1.5_10_10	1.5	10	10
M_1.5_10_15	1.5	10	15
M_2_2_15	2	2	15
M_2_4_15	2	4	15
M_2_6_10	2	6	10
M_2_6_15	2	6	15
M_2_6_20	2	6	20
M_2_10_10	2	10	10
M_2_10_15	2	10	15
M_2.5_10_10	2.5	10	10
M_2.5_10_15	2.5	10	15
M_3_2_15	3	2	15
M_3_4_15	3	4	15
M_3_6_10	3	6	10
M_3_6_15	3	6	15
M_3_6_20	3	6	20

In all the tests, a spot size of 2.5 mm, and an offset in the *Z*-axis of 0.2 mm were applied. High purity argon (99.99%), with a 5.5 L/min flow rate, was used as the shielding gas to prevent contamination and oxidation of the melt pool during the DLD process. Samples with and without PHT were cooled in air.

Samples from each deposition were cut for microstructural and mechanical characterization using a metallographic cut-off machine with refrigeration, to avoid substrate and cladding overheating. Samples were mounted in resin and polished down to 1 µm diamond suspension, and Kalling's No. 2 chemical etching ($CuCl_2$—5 g, Hydrochloric acid

—100 mL, Ethanol—100 mL) was used to reveal the microstructures. The measurements of height, depth and width of the claddings produced by the DLD technique were performed using a Leica DVM6 A 2019 digital microscope (DM) (Wetzlar, Germany). Leica DM 4000M optical microscope (OM) (Wetzlar, Germany) was used for the microstructural characterization of samples. OM analysis at low magnifications allows a global characterization of clads to evaluate, for example, the size of the heat-affected zone.

A scanning electron microscope (FEI Quanta 400 FEG ESEM, Hillsboro, OR, USA) equipped with Energy Dispersive X-Ray Spectroscopy (EDX) (EDAX Genesis X4M, Oxford Instrument, Oxfordshire, UK) and Electron backscatter diffraction (EBSD) (EDAX-TSL OIM EBSD, Mahwah, NJ, USA) units, was used for higher magnification observation and phase identification.

For EBSD evaluation, samples went through an additional polishing step, using a 0.06 μm silica colloidal suspension, for a superior surface finish and removal of polishing induced plastic deformation. This additional polishing is essential for obtaining Kikuchi patterns [31]. The EBSD allows obtaining information on microstructural characteristics with a small volume of interaction and high resolution. For all raw data, a dilatation clean-up routine was performed, with a grain tolerance angle of 15° and minimum grain size of 10 points, to avoid any spurious results from the incorrectly indexed patterns.

Vickers microhardness tests made the mechanical characterization. The tests were performed using a test force of 300 g for 15 s in a Struers Duramin 5 Vickers hardness tester. Each hardness value corresponds to the average of three indentations.

3. Results

3.1. Microstructural and Mechanical Characterization

The deposited clads characterization started with a macrographic observation to evaluate the effect of the processing conditions on the substrate and, mainly, on the geometry of the clad, its dilution, and eventual cracking (Figure 3). Different regions of this layer can be observed in Figure 3, such as the cladding layer (CL), the fusion line (FL), and the heat-affected zone (HAZ). The claddings produced must be strongly bonded to the substrate and free of discontinuities and cracks and must not induce them in the HAZ of the substrate.

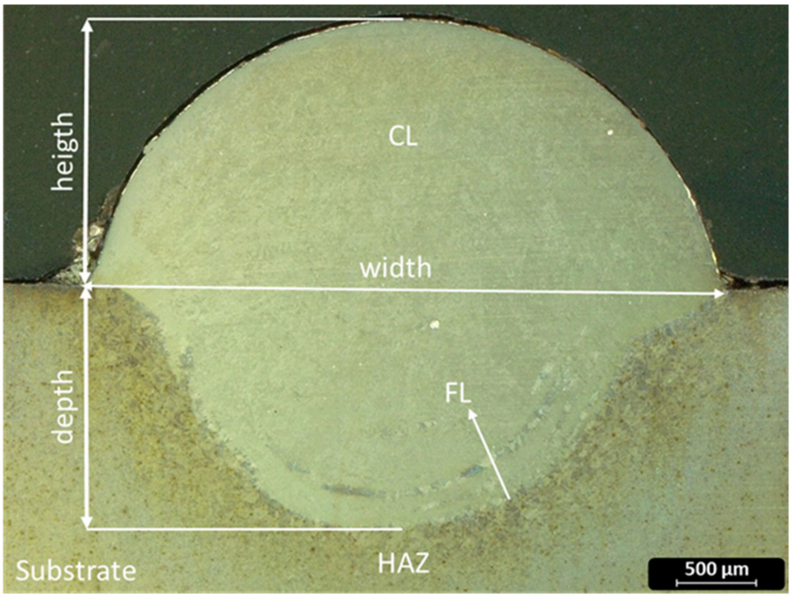

Figure 3. Optical microscopy image showing the morphology of a single-track clad produced by the DLD technique depositing Metco 42C powder on a 42CrMo4 steel substrate. CL—Cladding Layer; FL—Fusion Line; HAZ—Heat-affected Zone.

DM images allow the measurement of the clad (AC) and melting (AM) areas using ImageJ software. Tables 3 and 4 show the measurements made by DM of the length, height, and depth of the clad layers, for conditions with and without PHT, respectively.

Table 3. Dimensional analysis and dilution of clads produced by DLD without PHT. AC—Clad Area; AM—Melting Area.

Sample	Width (mm)	Height (mm)	Depth (mm)	AC (mm^2)	AM (mm^2)	Dilution (%)	Cracks
M1_2_15	3.420	2.360	0.000	6.76	0.00	0.0	No
M1_6_15	3.410	0.930	0.000	2.48	0.00	0.0	No
M1.5_10_10	3.200	0.520	0.120	1.16	0.22	16.0	No
M1.5_10_15	3.190	0.760	0.044	1.75	0.16	8.4	No
M2_2_15	3.510	2.860	1.330	9.47	3.00	24.1	No
M2_4_15	3.560	1.790	1.140	5.34	2.60	32.8	No
M2_6_10	3.370	0.880	1.170	2.20	2.29	51.1	No
M2_6_15	3.820	0.926	0.956	2.79	2.20	44.1	No
M2_6_20	3.580	1.083	0.970	3.07	1.74	36.2	No
M2_10_10	3.300	0.530	0.940	2.06	1.25	37.8	Yes
M2_10_15	3.350	0.790	0.680	1.19	1.64	58.0	Yes
M2.5_10_10	3.400	0.560	1.190	1.40	2.60	65.0	Yes
M2.5_10_15	3.340	0.770	1.050	1.91	2.11	52.4	No
M3_2_15	5.000	2.436	2.590	9.16	8.55	48.3	No
M3_4_15	4.950	1.282	1.673	3.64	4.14	53.2	No
M3_6_10	4.130	0.646	1.927	3.59	4.21	54.0	Yes
M3_6_15	3.870	1.061	1.910	2.17	6.15	74.0	Yes
M3_6_20	4.810	1.191	1.574	2.95	4.66	61.3	Yes

Table 4. Dimensional analysis and dilution of clads produced by DLD with PHT (300 °C). AC—Clad Area; AM—Melting Area.

Sample	Width (mm)	Height (mm)	Depth (mm)	AC (mm^2)	AM (mm^2)	Dilution (%)	Cracks
M1_2_15	3.720	2.224	0.000	7.43	0.00	0.0	No
M1_6_15	3.910	0.936	0.000	2.41	0.00	0.0	No
M1.5_10_10	3.430	0.490	0.074	1.21	1.36	53.0	No
M1.5_10_15	3.590	0.700	0.130	1.81	0.27	13.2	Yes
M2_2_15	4.180	2.830	1.890	10.38	4.84	31.8	No
M2_4_15	3.910	1.610	1.520	5.06	3.79	42.8	No
M2_6_10	3.600	0.890	1.550	2.33	3.31	58.7	No
M2_6_15	4.050	0.968	1.369	2.86	2.91	50.5	Yes
M2_6_20	3.780	1.241	1.312	3.52	2.83	44.5	Yes
M2_10_10	3.490	0.550	1.210	1.90	1.53	44.6	No
M2_10_15	3.460	0.760	0.880	1.39	2.38	63.2	Yes
M2.5_10_10	3.460	0.590	1.510	1.49	3.29	68.8	Yes
M2.5_10_15	3.460	0.790	1.320	1.92	2.58	57.4	Yes
M3_2_15	4.960	2.540	3.263	9.15	10.25	52.8	Yes
M3_4_15	5.190	1.342	2.289	4.66	8.18	63.7	Yes
M3_6_10	3.810	0.815	2.287	3.72	5.92	61.4	Yes
M3_6_15	3.860	1.105	2.018	2.29	6.24	73.1	Yes
M3_6_20	4.890	1.123	1.929	3.13	5.17	62.3	Yes

The microstructure of a clad deposited by the DLD process (Figure 4) is typical of this laser process, showing a thin zone of planar growth composed of equiaxed grains (EG) close to the fusion line that are replaced by dendrites (D) in the central region of the clad area. This microstructure is directly related to the process and thermal convection phenomena: the planar zone forms due to the high-temperature gradient, which reduced with deposition, increasing the solidification rate (super-cooling), and the microstructure evolves to a dendritic/columnar type, as reported in other studies [22,31]. The PHT affects the size of dendrites, and samples with PHT showed dendrites of greater thickness.

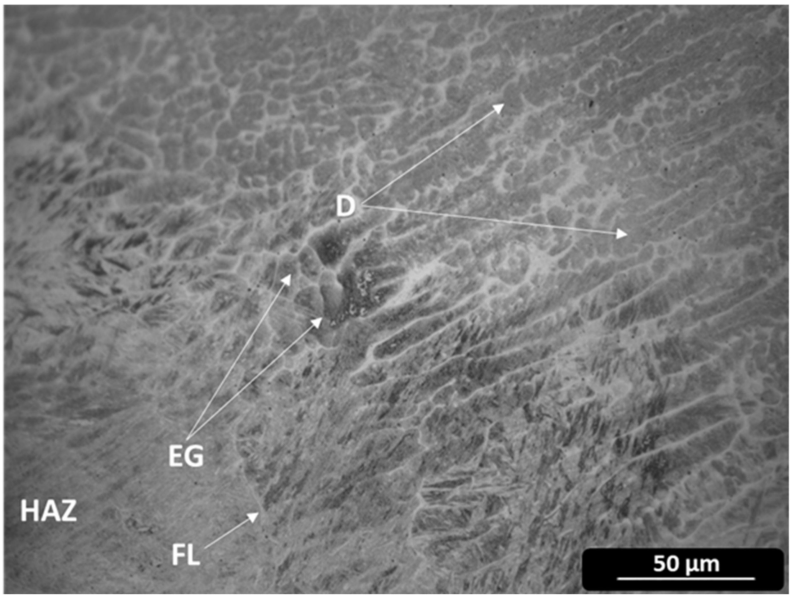

Figure 4. Optical microscopy image showing the solidification structure in the M2_6_15 sample. D—Dendrites; EG—Equiaxed Gains; FL—Fusion Line; HAZ—Heat-affected Zone.

The localized cooling rate in the DLD process promotes significant microstructural alteration in the HAZ region with the formation of Martensite (M). PHT at 300 °C reduced the temperature gradient (and the resulting cooling rate) and induces microstructural changes at HAZ, allowing the martensite laths to have larger dimensions and the formation of a higher amount of ferrite.

To evaluate the PHT effect, mechanical and microstructural analyses were concentrated in the interface region between CL and HAZ. The microstructure in these regions was characterized by SEM observations. The clad is mainly composed of martensite, with a random crystallographic orientation, and vermicular δ-ferrite surrounding the martensite laths (Figure 5). A low percentage of retained austenite was detected by the EBSD analysis.

The effect of δ-ferrite is already known and widely studied by researchers linked to the welding process, but not much researched in laser material processing. According to Niessen et al. [32], the presence of the δ-ferrite phase promotes a severe reduction of toughness and ductility. This phase increases ductile-to-brittle transition temperature (DBTT), deteriorating impact properties, and the formation of brittle cracks in the martensitic matrix [33]. This can be a determining factor in clad cracking (Figure 6), which is dependent on the processing conditions, mainly on the laser power, being more frequent and more extensive in samples with PHT (Figure 7).

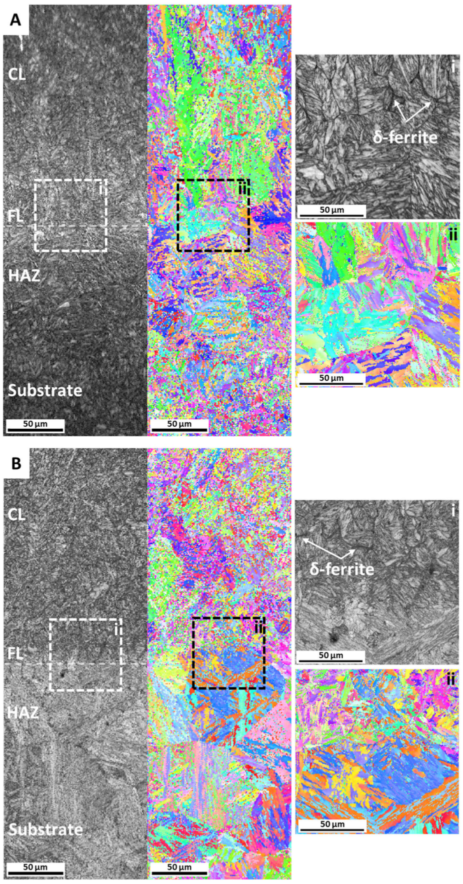

Figure 5. Electron backscatter diffraction (EBSD) images showing the microstructure of M2_6_15 samples (**A**) with and (**B**) without PHT.

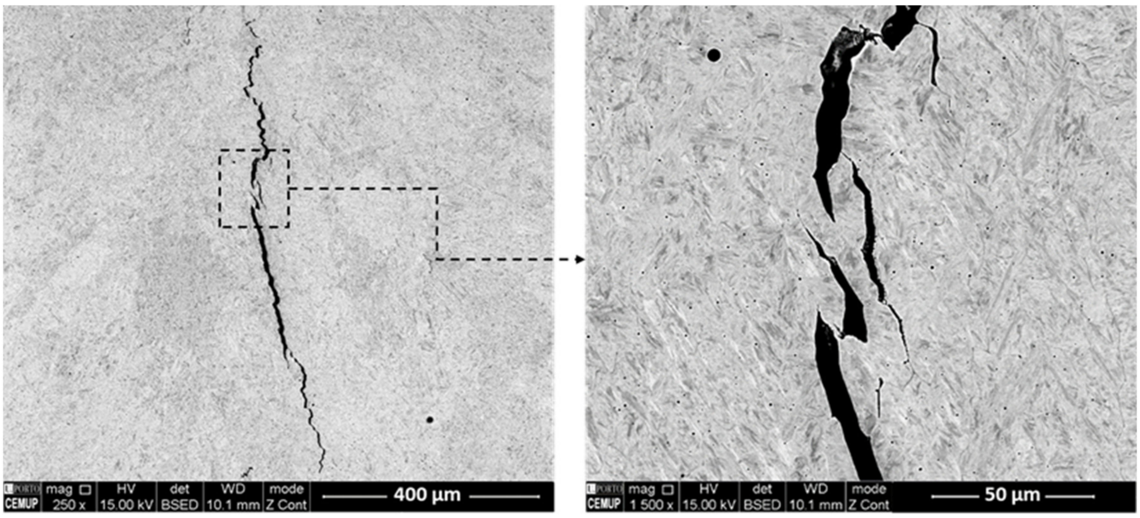

Figure 6. SEM images of cracks formed in the M2_6_15 sample with PHT.

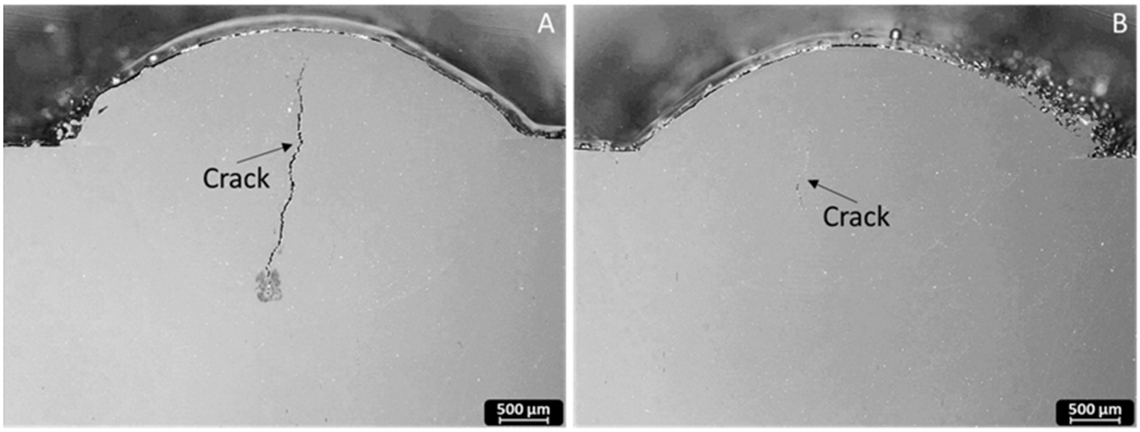

Figure 7. OM images of cracks formed in the centre of the cladding in M3_6_10 samples (**A**) with and (**B**) without PHT.

The influence of the PHT in microstructure has a direct consequence on mechanical behaviour. Microhardness profiles were determined to evaluate this influence on the mechanical response. Figure 8 shows microhardness evolution across the clad and substrate, including HAZ.

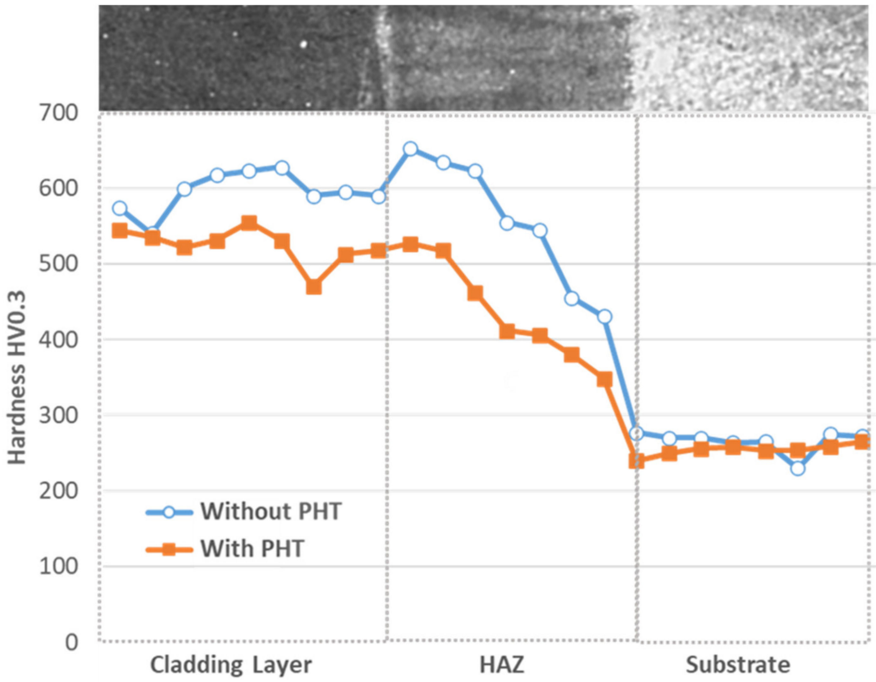

Figure 8. Microhardness profile of M2_6_15 samples with and without PHT.

PHT reduces the hardness of both the clad areas near the substrate and HAZ. In fact, in HAZ a maximum hardness of 652HV0.3 and 524HV0.3 were measured in the samples without and with PHT, respectively, showing a significant decrease in hardness due to substrate preheating. This hardness variation can be explained by the lower cooling rate of PHT samples and its effect on microstructure, mainly increasing the quantity of ferrite formed and allowing martensite tempering. A smooth hardness gradient in HAZ is crucial to increase the substrate crack propagation resistance.

The presented microstructures in Figures 4 and 5 are representative of all produced clads and it was difficult to select the best processing conditions based on microstructural or mechanical analysis.

3.2. Influence of Processing Conditions

According to the information described in Tables 2–4, all the processing parameters, such as laser power, scanning speed, powder feed rate, and preheating strongly influence the production, bonding, and quality of the cladding. The selection of processing conditions that ensures a clad without defects, bonded to the substrate and with good material yield, is an essential and challenging task because the various variables interaction. Their simultaneous optimization is difficult because they often act in opposite directions.

Dilution, which assesses the contribution of the substrate (area of the substrate that is melted by the laser) to the total area of the clad, is an important aspect of DLD clads. It allows the control of contamination of the clad by the substrate and affects the deposition yield. High dilutions can compromise the quality of the clad and increase distortion [34], but some dilution is necessary to ensure the metallurgical bond of the cladding to the substrate. With the measured clad and melting areas (Tables 3 and 4), dilution was determined using Equation (1). The dilution values are also shown in Tables 3 and 4.

$$\text{Dilution}\,(\%) = \text{AM}/(\text{AC} + \text{AM}) \times 100 \quad (1)$$

These results show that a laser power of 1 kW is enough to melt the powder and produce a clad. However, it is not sufficient to guarantee the metallurgical bonding of the clad to the substrate (dilution equal to 0%). The results in Tables 3 and 4 evidence that dilution increases with laser power.

However, the increase in laser power must be carefully performed because of its negative effect on clad soundness. Overheating, caused by an excessive energy input per unit area of the substrate, which is preheated, leads to an increase in residual stresses favouring the appearance of cracks in the cladding [34]. This also facilitates the formation of eutectic compounds resulting from the segregation of elements, such as silicon, for grain boundaries, and interdendritic regions [35]. In short, the thermal stresses generated by the PHT at 300 °C, high laser power and the presence of δ-ferrite most often cause cracks in samples with PHT, as evidenced in Tables 3 and 4.

Analysis of these data shows that keeping all other parameters equal, an increase in the feed rate causes an increase in the cladding height and usually a decrease in its depth. A higher feed rate implies a more significant amount of powder ejected from the coaxial nozzle in the same period; the powder particles will form a denser cloud, absorbing more of the beam energy of the laser resulting in a higher deposition rate (higher clads).

For the same feed rate, PHT produces clads with greater height and depth in most cases. This effect can be explained by the forced thermal convection phenomenon, with the samples with PHT having a higher internal heat and, consequently, allowing greater powder melting. Another contribution of PHT is the increase in the laser absorption rate by the substrate [36], making the melt pool more fluid, which allows a more significant deposition of the powder and increases the penetration depth, thus increasing the dilution.

Scanning speed affects the morphology of claddings produced by DLD, depending on the specific energy of the laser and the interaction with powder cloud. When the scanning speed is small, the mass of deposited powder per unit of length, and consequently the volume of the formed clad, is quite large due to the interaction for a more extended period between the laser beam and the powder. However, if the speed is higher, the interaction between the laser beam and the powder cloud will be less, decreasing the amount of deposited material. Increasing the scanning speed decreases the powder, and the energy deposited per unit length and melt pool volume [18].

Tables 3 and 4 show that lower scanning speed typically produces coatings with greater heights and depths. The greater depth is due to the more extended interaction of the laser beam with the substrate. PHT also increases the depth due to the Marangoni convection effect. This effect is caused by the surface tension gradient, which becomes more evident with increasing substrate temperature [11].

Although this detailed analysis of the individual effect of these three variables (scanning speed, laser power, and feed rate) is essential to clarify their role in the deposition of Metco42C on a 42CrMo4 steel substrate, the effect of each is difficult to isolate. It is necessary to apply combined parameters to obtain a more accurate relationship between processing and clad characteristics.

Powder Deposition Density (PDD) is a widely used parameter that can express the combined influence of feed rate, scanning speed, and laser spot size (φ) [37,38]. The powder deposition density is defined by Equation (2). Figure 9 shows that the cladding area increases linearly with the increase in the PDD parameter and that PHT has a negligible influence on this relationship.

$$\mathrm{PDD}\Big(\mathrm{g/mm^2} = \mathrm{FR}/(\mathrm{SS}\ \varphi) \quad (2)$$

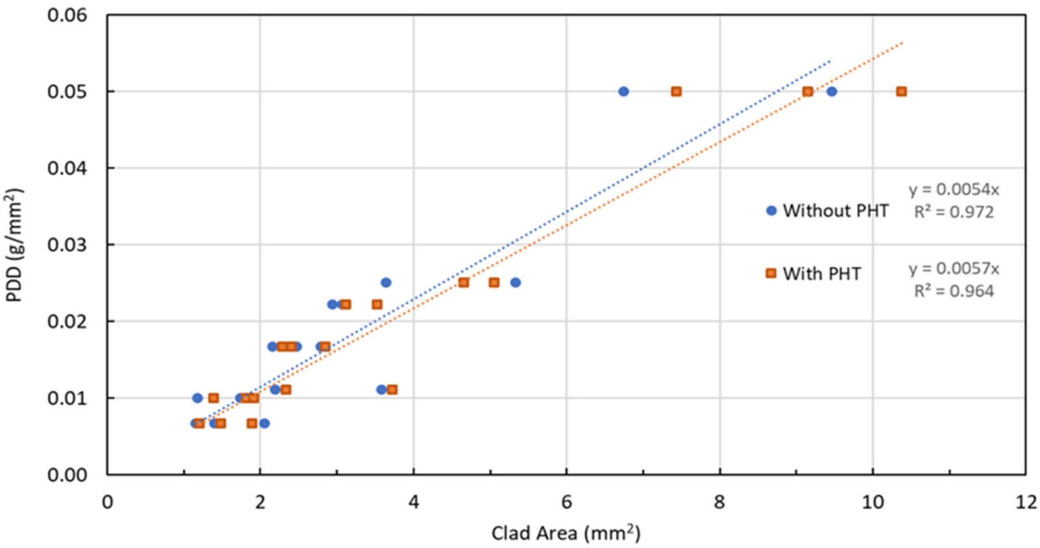

Figure 9. Relationship between the cladding area and the value of the PDD parameter.

A similar analysis was performed in which the three analyzed processing parameters (Laser power—P, Scanning speed—SS, and Feed rate—FR) were merged in an empirical combined parameter P*SS/FR [16] and correlated with the dilution (Figure 10).

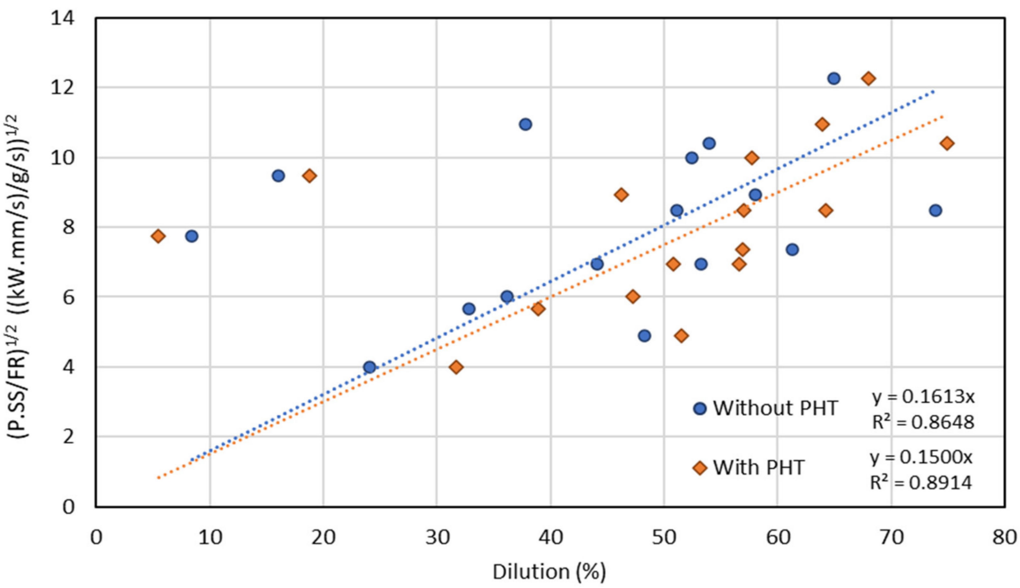

Figure 10. Dependence of dilution on the value of complex parameter P*SS/FR.

As shown in Figure 10, PHT promoted a greater dilution compared to samples without PHT. As discussed above, this influence is mainly controlled by the Marangoni convection effect caused by the surface tension gradient.

It was more challenging to find a complex parameter that would allow the processing conditions to be associated with the appearance of cracks. This relationship was achieved when using $P^4 \cdot SS^2/FR$ as a complex parameter (Figure 11). The limit values of 2000 and 5000 $(kW)^4 \cdot (mm/s)^2/(g/s)$ allow the production of sound clads in samples with and without PHT, respectively.

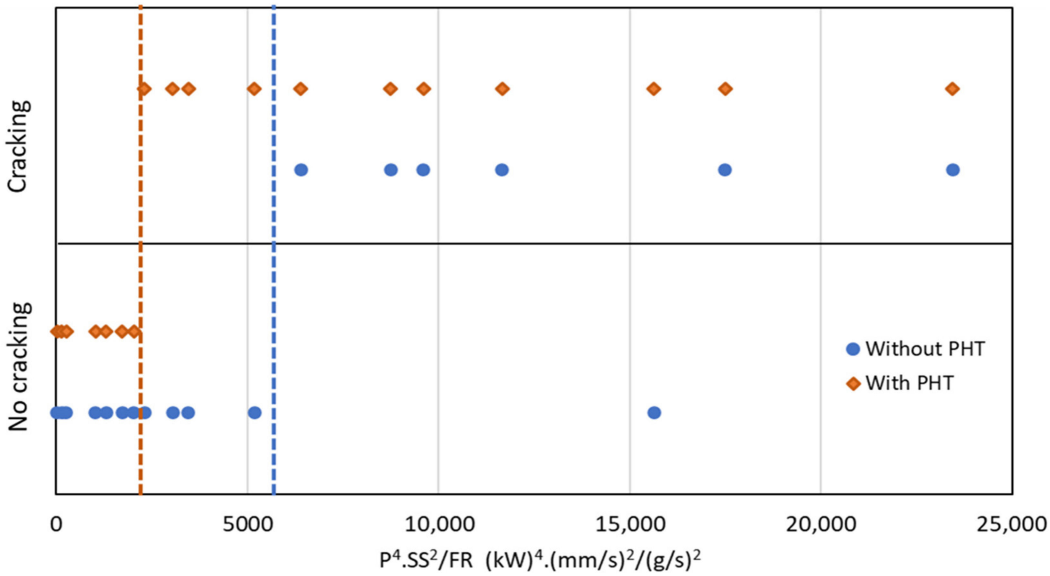

Figure 11. Relationship between the processing parameters expressed by the $P^4 \cdot SS^2/FR$ complex parameter in the formation of cracks.

3.3. Optimization of Processing Conditions

The complex interaction between the processing parameters, which implied the need to use complex parameters that must be adjusted to each process, makes it essential to apply an optimization algorithm. Optimization is an approach towards the best state among possible solutions that involves selection among many responses. Since there are constraints in real problems, generally just a better response is selected instead of the best one.

The interaction and interdependence of the different process variables led to applying a Genetic Optimization Algorithm to select a response in which the objective functions obtain the best-desired response. This multi-objective optimization problem is dynamic and is supported and validated with the experimental results [39,40].

In this study, the Response Surface Model (RSM) was used to calculate the ideal combination of laser power and scanning speed that minimizes the values of the height and depth of the clad and ensures a 10% dilution while guaranteeing sound clads with bonding to the substrate. These conditions make it possible to produce strands with a good wettability (minimizing height) and maximizing the yield of the deposition process (minimizing depth and dilution). The presented results are for a constant feed rate of 15 g/min. This feed rate was selected as the best after the first series of experimental results.

In the Response Surface Model (RSM), objective functions are derived considering different laser powers (x) and scanning speeds (y) as inputs, and using genetic algorithms, optimum values for these functions are specified, considering the constraints. Two polynomial models were defined, without and with preheating condition, the objective functions are shown in Equations (3)–(5) and Equations (6)–(8), respectively.

Without preheating:

$$obj_{height}(x,y) = 2560 + 1770{*}x - 723.6{*}y - 434.2 * x^2 - 190.7{*}x * y + 70.4 * y^2 + 41.1 * x^2{*}y + 2.976 * x * y^2 - 1.851 * y^3 \quad (3)$$

$$obj_{depth}(x,y) = -1774 + 2597{*}x - 145.2{*}y - 258.7 * x^2 - 368.8{*}x * y + 92.09 * y^2 + 43.44 * x^2{*}y + 12.62 * x * y^2 - 6.433 * y^3 \quad (4)$$

$$obj_{dilution}(x,y) = 791.3 - 1806 * x - 4.99 * y + 1424 * x^2 + 7.405 * x * y - 463.8 * x^3 - 2.844 * x^2 * y + 54.08 * x^4 + 0.3654 * x^3 * y \quad (5)$$

With preheating:

$$obj_{height}(x,y) = 2117 + 2917 * x - 1046 * y - 670.3 * x^2 - 470.2 * x * y + 184.8 * y^2 + 104.7 * x^2 * y + 3.83 * x * y^2 - 8.149 * y^3 \quad (6)$$

$$obj_{depth}(x,y) = -2352 + 3157 * x - 199.2 * y - 226 * x^2 - 248.2 * x * y + 82.54 * y^2 - 29.85 * x^2 * y + 26.23 * x * y^2 - 7.545 * y^3 \quad (7)$$

$$obj_{dilution}(x,y) = -35.85 + 34.75 * x - 10.71 * y - 1.294 * x^2 + 15.89 * x * y + 0.1334 * y^2 - 4.257 * x^2 * y + 0.2834 * x * y^2 - 0.08753 * y^3 \quad (8)$$

The fitted curves for Equations (3)–(5) are shown in Figures 12–14, respectively. Data validation is verified using the Matlab software and curve-fitting toolbox. When variables are selected, the mentioned toolbox can calculate validation statistics such as Root Mean Squared Error (RMSE), and the best fitting has the least amount of RMSE. The same approach was used to fit the curves for the condition of without preheating.

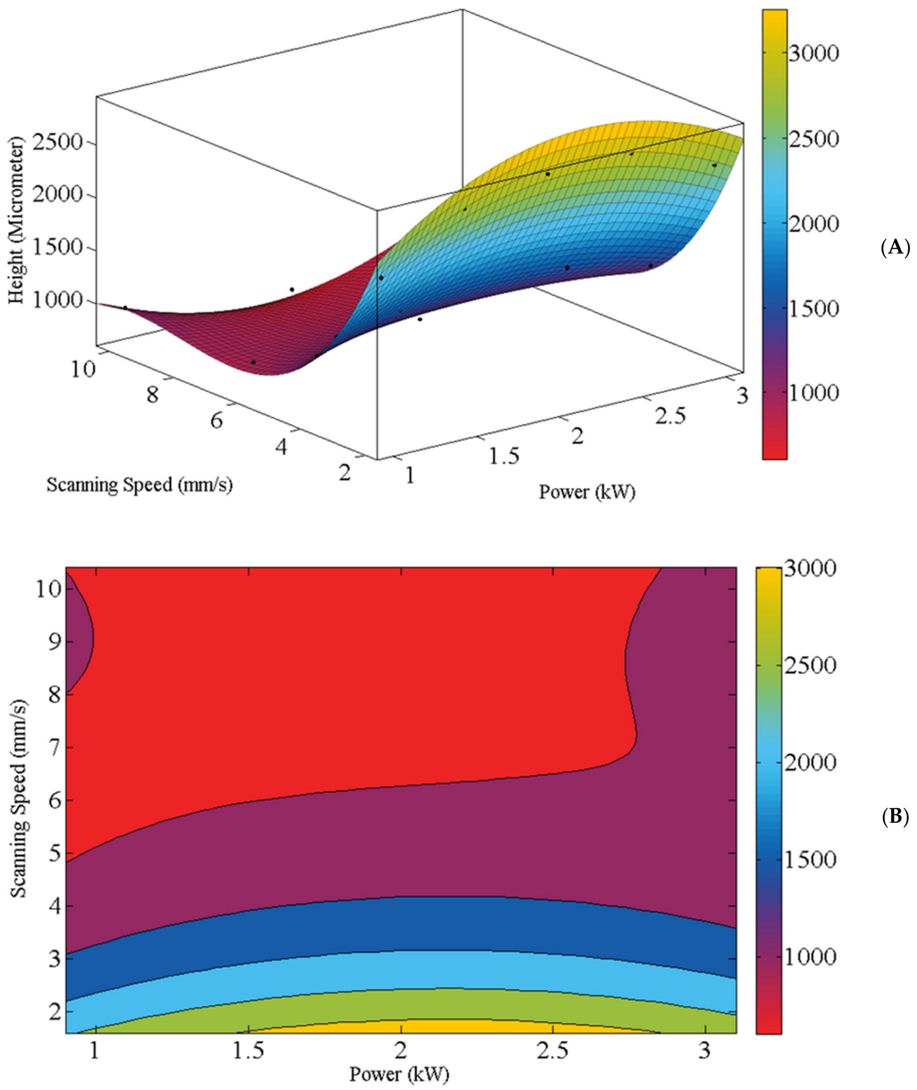

Figure 12. (**A**) The best curved surface (R-square: 0.9908; Adjusted R-square: 0.9539; RMSE: 0.1347) and (**B**) contour plot for the height (in micrometers) of deposited clad regarding the combination of the laser power and scanning speed.

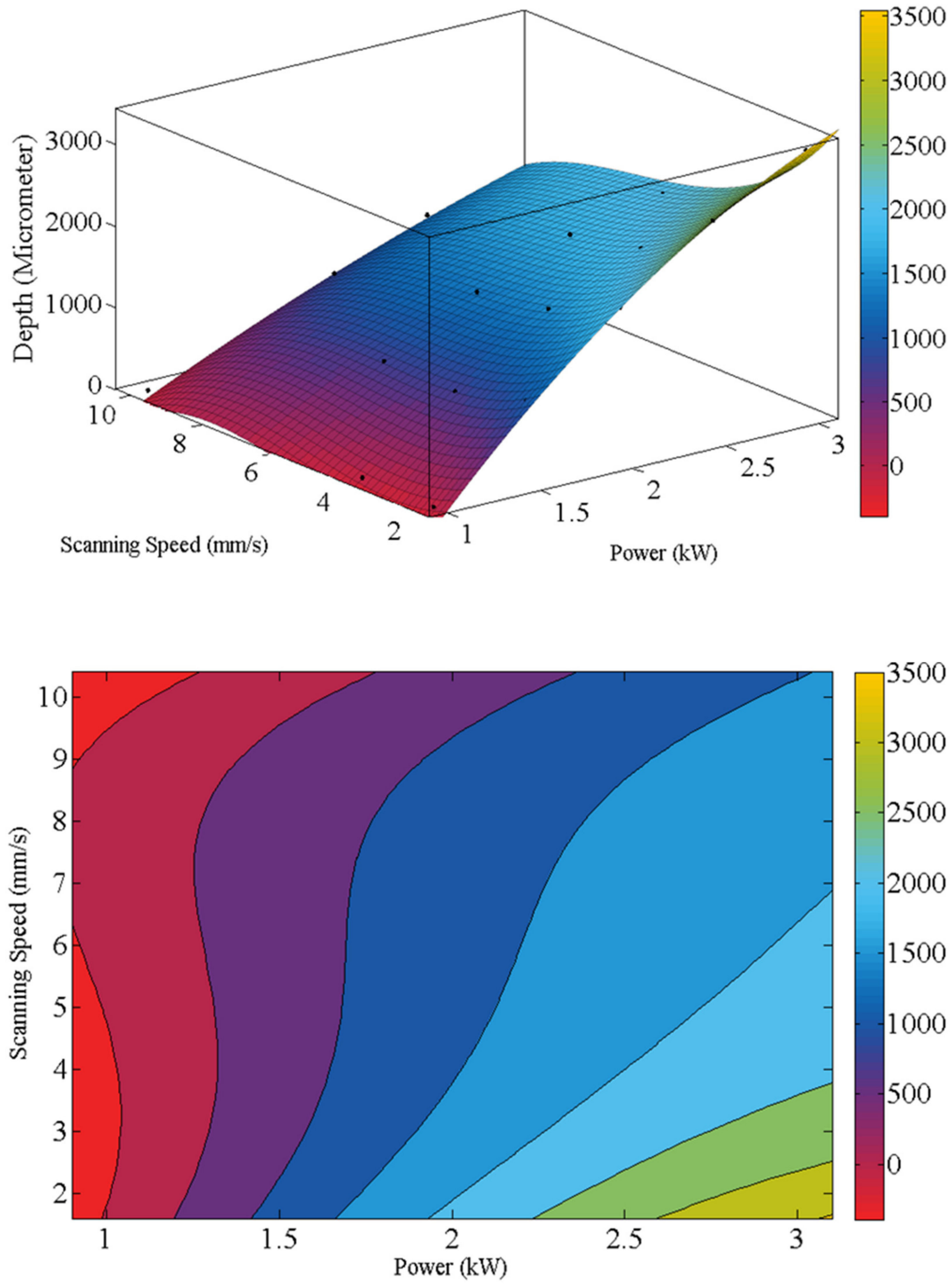

(**A**)

(**B**)

Figure 13. (**A**) The best curved surface (R-square: 0.9904; Adjusted R-square: 0.952; RMSE: 0.1674) and (**B**) contour plot for the depth (in micrometers) of deposited clad regarding the combination of the laser power and scanning speed.

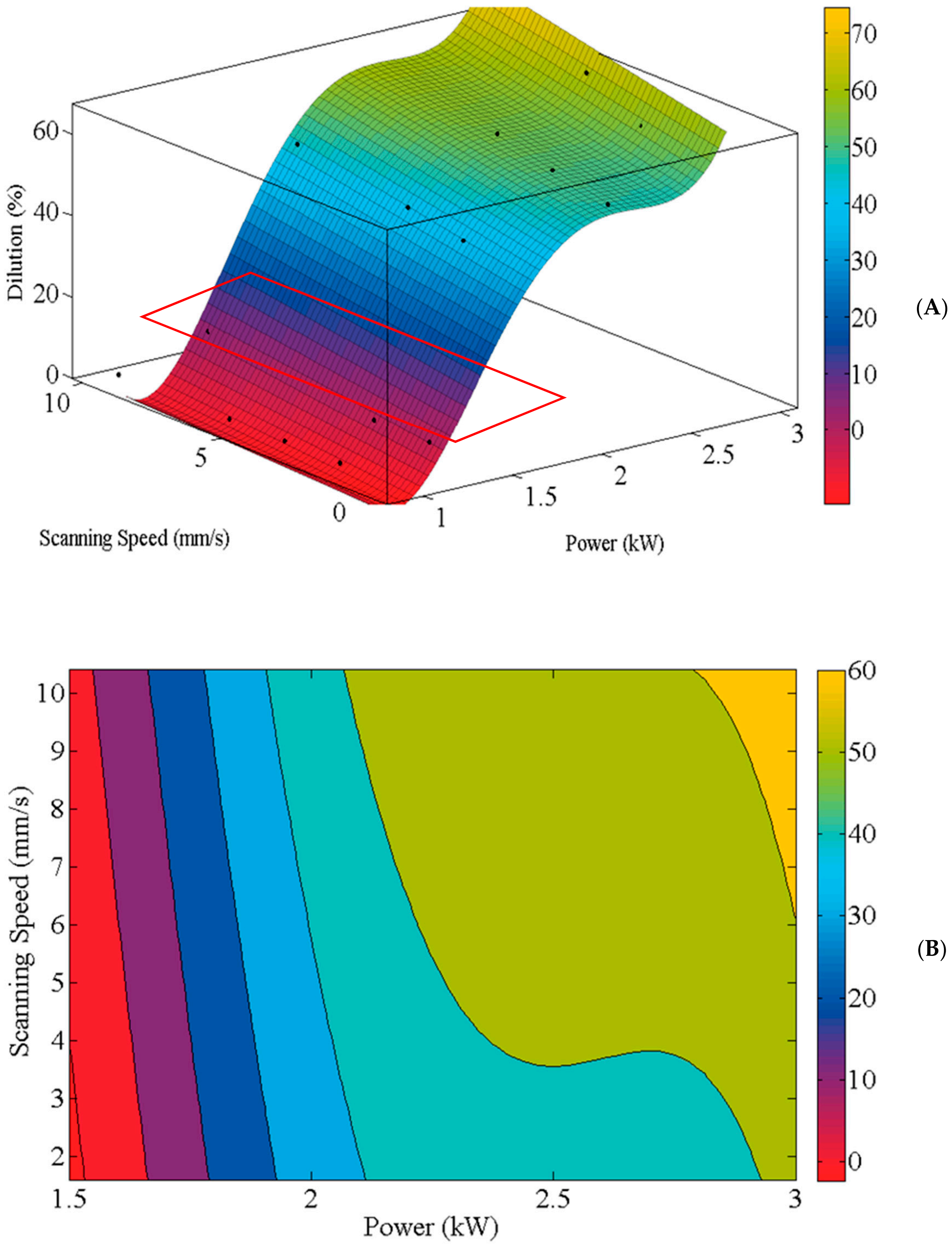

Figure 14. (**A**) The best curved surface (R-square: 0.9728; Adjusted R-square: 0.8641; RMSE: 0.347) and (**B**) contour plot for the dilution (in %) of deposited clad regarding the combination of the laser power and scanning speed.

Figures 15 and 16 illustrate derived Pareto frontiers [38] minimizing the three objective functions simultaneously for samples without preheating and with 300 °C preheating, respectively.

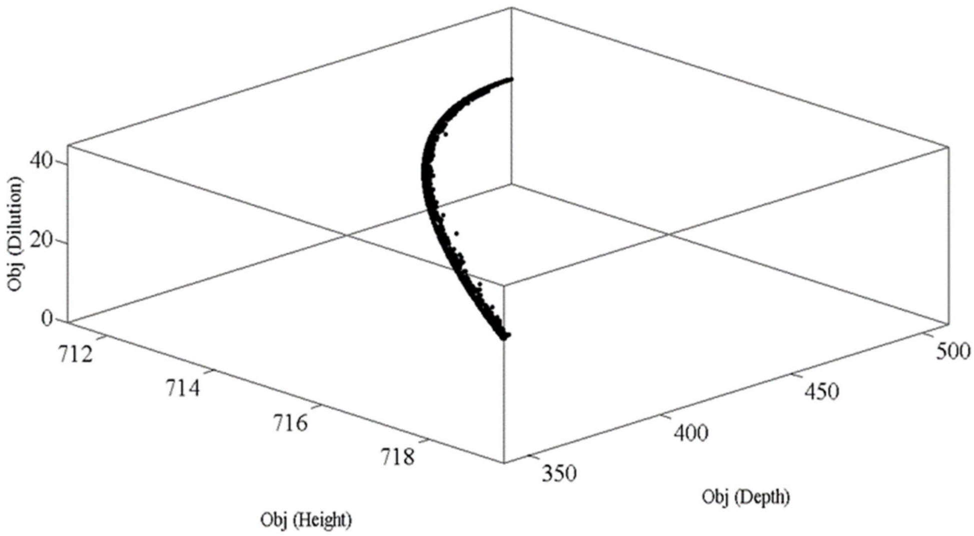

Figure 15. 3D Pareto frontier of the three objective functions including depth, dilution, and height of clads, with a feed rate of 15 g/min and without pre-heating.

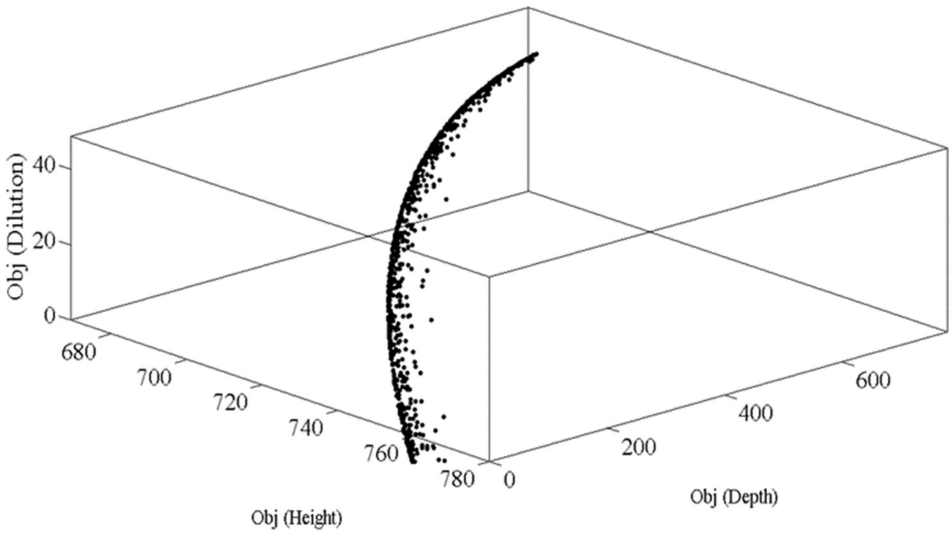

Figure 16. 3D Pareto frontier of the three objective functions including depth, dilution, and height of clads, with a feed rate of 15 g/min and with 300 °C pre-heating.

In this study, L3 norm Minimization technique [41] is used to minimize the distance from the Pareto set to an ideal solution, utopia point. Table 5 shows the best values for minimized outputs based on the inputs. For a feed rate of 15 g/min, the best processing conditions are a scan speed of 10 mm/s and a laser power of 1.5 and 1.7 kW for samples with and without preheating, respectively. These values correspond to 3340 and 2025 $(kW)^4{\cdot}(mm/s)^2/(g/s)$, which are in accordance with those determined by using the empirical complex parameter $P^4{\cdot}SS^2/FR$.

Table 5. Optimized value of the inputs and outputs for a feed rate of 15 g/min.

Conditions	Laser Power (kW)	Scan Speed (mm/s)	Height (μm)	Depth (μm)	Dilution (%)
Without preheating	1.70	10.000	719	348	28.3
With preheating	1.49	9.999	734	123	16.7

4. Conclusions

The present study analyzed the effect of laser power, scan speed, and feed rate on the deposition of AISI 431 steel powder (Metco 42C) on a 42CrMo4 steel substrate. The analysis of the clads revealed a martensitic structure with delta ferrite. This structure is susceptible to the appearance of cracks in the cladding area, this cracking being more common when the substrates were preheated to 300 °C. The metallurgical bonding of the clad to the substrate requires a power greater than 1 kW. Laser powers greater than 2 or 1.5 kW, for samples without or with preheating, respectively, induce dilutions greater than 30% with the consequent decrease in the yield of the deposition process. The increase in laser power and scan speed increases the possibility of cracking. The use of experimental complex parameters made it possible to define the conditions that prevent cracking and guarantee a sound clad with good deposition yield. The values obtained are 2000 and 5000 $(\mathrm{kW})^4\cdot(\mathrm{mm/s})^2/(\mathrm{g/s})$ in samples with and without PHT, respectively. The use of a genetic optimization algorithm indicated that the best processing conditions were obtained with speeds of 10 mm/s, feed rate of 15 g/min, and laser powers of 1.5 and 1.7 kW for samples with and without preheating, respectively. These conditions agree with the ones resulting from the application of the complex parameters.

Author Contributions: A.A.F., M.F.V. and A.R.R. proposed the methodology and results data analyses followed in this research, A.A.F., J.P.S. and J.M.C. carried out the experimental tests, R.D. performed the genetic optimization and all authors participated in the discussion of results and writing of the manuscript. All authors have read and agreed to the published version of the manuscript.

Funding: This research was funded by FEDER through the program P2020 | COMPETE, Projetos em Copromoção (project POCI-01-0247-FEDER-039848).

Institutional Review Board Statement: Not applicable.

Informed Consent Statement: Not applicable.

Data Availability Statement: Not applicable.

Acknowledgments: The authors are grateful to CEMUP (Centro de Materiais da Universidade do Porto) for expert assistance with SEM, and to Project ADDing (POCI-01-0145-FEDER-030490), co-financed by FEDER through P2020 | COMPETE and national funds through Fundação para a Ciência e a Tecnologia.

Conflicts of Interest: The authors declare no conflict of interest.

References

1. Alimardani, M.; Fallah, V.; Khajepour, A.; Toyserkani, E. The effect of localized dynamic surface preheating in laser cladding of Stellite 1. *Surf. Coat. Technol.* **2010**, *204*, 3911–3919. [CrossRef]
2. Leunda, J.; Navas, V.G.; Soriano, C.; Sanz, C. Effect of laser tempering of high alloy powder metallurgical tool steels after laser cladding. *Surf. Coat. Technol.* **2014**, *259*, 570–576. [CrossRef]
3. Dass, A.; Moridi, A. State of the Art in Directed Energy Deposition: From Additive Manufacturing to Materials Design. *Coatings* **2019**, *9*, 418. [CrossRef]
4. Thompson, S.M.; Bian, L.; Shamsaei, N.; Yadollahi, A. An overview of Direct Laser Deposition for additive manufacturing; Part I: Transport phenomena, modeling and diagnostics. *Addit. Manuf.* **2015**, *8*, 36–62. [CrossRef]
5. Vilar, R.; Santos, E.; Ferreira, P.; Franco, N.; Da Silva, R. Structure of NiCrAlY coatings deposited on single-crystal alloy turbine blade material by laser cladding. *Acta Mater.* **2009**, *57*, 5292–5302. [CrossRef]
6. Fu, F.; Zhang, Y.; Chang, G.; Dai, J. Analysis on the physical mechanism of laser cladding crack and its influence factors. *Optik* **2016**, *127*, 200–202. [CrossRef]
7. Hutasoit, N.; Luzin, V.; Blicblau, A.; Yan, W.; Brandt, M.; Cottam, R. Fatigue life of laser clad hardfacing alloys on AISI 4130 steel under rotary bending fatigue test. *Int. J. Fatigue* **2015**, *72*, 42–52. [CrossRef]
8. Chen, J.-Y.; Conlon, K.; Xue, L.; Rogge, R. Experimental study of residual stresses in laser clad AISI P20 tool steel on pre-hardened wrought P20 substrate. *Mater. Sci. Eng. A* **2010**, *527*, 7265–7273. [CrossRef]
9. Brandl, E.; Michailov, V.; Viehweger, B.; Leyens, C. Deposition of Ti–6Al–4V using laser and wire, part II: Hardness and dimensions of single beads. *Surf. Coat. Technol.* **2011**, *206*, 1130–1141. [CrossRef]
10. Le, T.-N.; Lo, Y.-L. Effects of sulfur concentration and Marangoni convection on melt-pool formation in transition mode of selective laser melting process. *Mater. Des.* **2019**, *179*, 107866. [CrossRef]

11. Jiang, Y.; Cheng, Y.; Zhang, X.; Yang, J.; Yang, X.; Cheng, Z. Simulation and experimental investigations on the effect of Marangoni convection on thermal field during laser cladding process. *Optik* **2020**, *203*, 164044. [CrossRef]
12. Ju, J.; Zhou, Y.; Kang, M.; Wang, J. Optimization of Process Parameters, Microstructure, and Properties of Laser Cladding Fe-Based Alloy on 42CrMo Steel Roller. *Material* **2018**, *11*, 2061. [CrossRef] [PubMed]
13. Huang, C.; Lin, X.; Yang, H.; Liu, F.; Huang, W. Microstructure and Tribological Properties of Laser Forming Repaired 34CrNiMo6 Steel. *Material* **2018**, *11*, 1722. [CrossRef] [PubMed]
14. Dai, Q.-L.; Luo, C.-B.; You, F.-Y. Crack Restraining Methods and their Effects on the Microstructures and Properties of Laser Cladded WC/Fe Coatings. *Material* **2018**, *11*, 2541. [CrossRef]
15. Ocylok, S.; Alexeev, E.; Mann, S.; Weisheit, A.; Wissenbach, K.; Kelbassa, I. Correlations of Melt Pool Geometry and Process Parameters During Laser Metal Deposition by Coaxial Process Monitoring. *Phys. Procedia* **2014**, *56*, 228–238. [CrossRef]
16. Ocelík, V.; De Oliveira, U.; De Boer, M.; De Hosson, J.T.M. Thick Co-based coating on cast iron by side laser cladding: Analysis of processing conditions and coating properties. *Surf. Coat. Technol.* **2007**, *201*, 5875–5883. [CrossRef]
17. De Oliveira, U.; Ocelík, V.; De Hosson, J. Analysis of coaxial laser cladding processing conditions. *Surf. Coat. Technol.* **2005**, *197*, 127–136. [CrossRef]
18. Huang, Y. Characterization of dilution action in laser-induction hybrid cladding. *Opt. Laser Technol.* **2011**, *43*, 965–973. [CrossRef]
19. Gao, J.; Wu, C.; Hao, Y.; Xu, X.; Guo, L. Numerical simulation and experimental investigation on three-dimensional modelling of single-track geometry and temperature evolution by laser cladding. *Opt. Laser Technol.* **2020**, *129*, 106287. [CrossRef]
20. Zhao, Y.; Guan, C.; Chen, L.; Sun, J.; Yu, T. Effect of process parameters on the cladding track geometry fabricated by laser cladding. *Optik* **2020**, *223*, 165447. [CrossRef]
21. Bi, G.; Gasser, A.; Wissenbach, K.; Drenker, A.; Poprawe, R. Identification and qualification of temperature signal for monitoring and control in laser cladding. *Opt. Lasers Eng.* **2006**, *44*, 1348–1359. [CrossRef]
22. Hemmati, I.; Ocelík, V.; De Hosson, J.T.M. Microstructural characterization of AISI 431 martensitic stainless steel laser-deposited coatings. *J. Mater. Sci.* **2011**, *46*, 3405–3414. [CrossRef]
23. Altuncu, E.; Tarım, M. Laser Cladding of Martensitic Stainless Steels on Armor Steels. *Emerg. Mater. Res.* **2020**, *9*, 1–4. [CrossRef]
24. Hemmati, I.; Ocelík, V.; De Hosson, J.T.M. The effect of cladding speed on phase constitution and properties of AISI 431 stainless steel laser deposited coatings. *Surf. Coat. Technol.* **2011**, *205*, 5235–5239. [CrossRef]
25. Li, L.; Shen, F.; Zhou, Y.; Tao, W. Comparative study of stainless steel AISI 431 coatings prepared by extreme-high-speed and conventional laser cladding. *J. Laser Appl.* **2019**, *31*, 042009. [CrossRef]
26. Ravi, G.; Hao, X.; Wain, N.; Wu, X.; Attallah, M. Direct laser fabrication of three dimensional components using SC420 stainless steel. *Mater. Des.* **2013**, *47*, 731–736. [CrossRef]
27. Shen, F.; Tao, W.; Li, L.; Zhou, Y.; Wang, W.; Wang, S. Effect of microstructure on the corrosion resistance of coatings by extreme high speed laser cladding. *Appl. Surf. Sci.* **2020**, *517*, 146085. [CrossRef]
28. Sun, C.; Fu, P.-X.; Liu, H.-W.; Liu, H.-H.; Du, N.-Y. Effect of Tempering Temperature on the Low Temperature Impact Toughness of 42CrMo4-V Steel. *Metals* **2018**, *8*, 232. [CrossRef]
29. International Conference on Recent Trends in Physics 2016 (ICRTP2016). *J. Phys. Conf. Ser.* **2016**, *755*, 011001. [CrossRef]
30. *BS EN 10269:2013: Steels and Nickel Alloys for Fasteners with Specified Elevated and or Low Temperature Properties*; BSI Standards Limited: London, UK, 2013; p. 6784 5. ISBN 978 0 580 76784 5.
31. Kurz, W.; Bezençon, C.; Gäumann, M. Columnar to equiaxed transition in solidification processing. *Sci. Technol. Adv. Mater.* **2001**, *2*, 185–191. [CrossRef]
32. Niessen, F.; Tiedje, N.S.; Hald, J. Kinetics modeling of delta-ferrite formation and retainment during casting of supermartensitic stainless steel. *Mater. Des.* **2017**, *118*, 138–145. [CrossRef]
33. Tabernero, I.; Lamikiz, A.; Martínez, S.; Ukar, E.; de Lacalle, L.L. Modelling of energy attenuation due to powder flow-laser beam interaction during laser cladding process. *J. Mater. Process. Technol.* **2012**, *212*, 516–522. [CrossRef]
34. Bennett, J.; Dudas, R.; Cao, J.; Ehmann, K.; Hyatt, G. Control of heating and cooling for direct laser deposition repair of cast iron components. In Proceedings of the 2016 International Symposium on Flexible Automation (ISFA), Cleveland, OH, USA, 1–3 August 2016; pp. 229–236.
35. Chen, Y.; Lu, F.; Zhang, K.; Nie, P.; Hosseini, S.R.E.; Feng, K.; Li, Z. Dendritic microstructure and hot cracking of laser additive manufactured Inconel 718 under improved base cooling. *J. Alloy. Compd.* **2016**, *670*, 312–321. [CrossRef]
36. Su, J.; Qiu, X.; Xing, F.; Ruan, Y. Effect of Preheating Temperature on Microstructure and Properties of 42CrMo4/38MnVS6 Heterogeneous Laser Welded Joint. *Metals* **2019**, *9*, 870. [CrossRef]
37. Toyserkani, E.; Khajepour, A.; Corbin, S.F. *Laser Cladding*; CRC Press: Boca Raton, FL, USA, 2004.
38. Farshidianfar, M.H.; Khajepour, A.; Gerlich, A.P. Effect of real-time cooling rate on microstructure in Laser Additive Manufacturing. *J. Mater. Process. Technol.* **2016**, *231*, 468–478. [CrossRef]
39. Nikam, S.H.; Jain, N.K.; Sawant, M.S. Optimization of parameters of micro-plasma transferred arc additive manufacturing process using real coded genetic algorithm. *Int. J. Adv. Manuf. Technol.* **2020**, *106*, 1239–1252. [CrossRef]
40. Zhang, K.; Chen, Y.; Zheng, J.; Huang, J.; Tang, X. Adaptive filling modeling of butt joints using genetic algorithm and neural network for laser welding with filler wire. *J. Manuf. Process.* **2017**, *30*, 553–561. [CrossRef]
41. Kasprzak, E.; Lewis, K. Pareto analysis in multiobjective optimization using the collinearity theorem and scaling method. *Struct. Multidiscip. Optim.* **2001**, *22*, 208–218. [CrossRef]